Iracheta, Omar and Bennett, Chris and Sun, Wei (2015) A sensitivity study of parameters affecting residual stress predictions in finite element modelling of the inertia friction welding process. International Journal of Solids and Structures, 71 . pp. 180-193. ISSN 0020-7683

A sensitivity study of parameters affecting residual stress predictions in finite element modelling of the inertia friction welding process

O. Iracheta, C. J. Bennett*, W. Sun

Department of Mechanical, Materials and Manufacturing Engineering,
University of Nottingham, Nottingham NG7 2RD, United Kingdom

* Corresponding author. E-mail address: chris.bennett@nottingham.ac.uk

Keywords: inertia friction welding, finite element analysis, transformation strain, residual stress

Abstract

This study presents a finite element (FE) model capable of predicting the final residual stress field in an inertia friction welded component of a CrMoV steel considering the elastic and inelastic components of strain resulting from mechanical deformation, temperature changes in the material and volumetric changes associated with phase transformations. The material database was improved to include the properties of the child phases involved in the polymorphic transformation during inertia friction welding (IFW) of CrMoV steels, i.e. austenite and quenched martensite, taking different approaches based on existent experimental data from the parent phase (tempered martensite) and material characterization of the heat affected zone (HAZ) in weld trials. This is the only FE model available in the literature that takes into consideration the effects induced by the transformation strain component of multiple phases in the total strain generated during IFW. Several simulations were run using this FE model in order to address for the first time the sensitivity of the final residual stress field to the individual effects of the microstructural changes, the interrelationship of multiple phases, and to different processing parameters such as the die geometry, clamping history and cooling rates.

Notation

A_c	Contact area
A_{c1}, A_{c3}	Temperatures in the equilibrium phase diagram at which austenite begins to

	form during heating (lower critical temperature) and at completion of austenite transformation (upper critical temperature)
A_{gauge}	Gauge area
A_{r3}	Temperature in the equilibrium phase diagram at which austenite begins to transform to ferrite during cooling
A, D	Martensitic transformation constants
E_k	Kinetic energy
F	Axial load during welding
f_s	Surface traction
h_c	Convection coefficient
I	Moment of inertia
K_c	Thermal conductivity of the workpiece
K	Incompressibility penalty constant
n	Simulation time step
$PSIg$	Gauge pressure
p	Normal pressure during welding
q_f	Frictional heat flux
r_i, r_o	Inner and outer radii at the contact of the weld interface
$\bar{T}$	Torque
T	Average element temperature
T_{Ae}, T_{As}	Austenite transformation end and start temperatures
T_e, T_s	Environment and surface temperatures
t	Time
u	Nodal velocity
V	Volume of the workpiece
β_{IJ}	Fractional length change due to transformation from phase I to phase J
δ_{ij}	Kronecker delta
ε_e, ε_p, ε_T	Elastic, plastic and thermal strain components
${\varepsilon^{Tr}}_{IJ}$	Transformation strain from phase I to phase J
$\dot{\bar{\varepsilon}}$	Effective strain rate
$\dot{\bar{\varepsilon}}_0$	Limiting strain rate
$\dot{\varepsilon}_{ij}$	Deviatoric strain rate
${\dot{\varepsilon}^{Tr}}_{IJ}$	Transformation strain rate
μ	Coulomb friction coefficient

ξ	Emissivity
ξ_J	Austenite volume fraction
$\dot{\xi}_J$	Transformation volume fraction rate
ξ_M	Martensite volume fraction
π	Work rate function
ρ	Material density
σ	Stefan-Boltzmann constant
$\bar{\sigma}$	Flow stress
σ_1, σ_2, σ_3	Principal stresses
σ'_{ij}	Deviatoric stress
$\bar{\sigma}_0$	Flow stress as a function of effective strain and limiting strain rate
τ_{fric}	Frictional shear stress
ψ_1, ψ_4	Austenitic transformation constants
ω	Angular velocity

1 Introduction

The increasing industrial demand of multi-material components engineered to fully exploit base properties of different materials so as to withstand different conditions at specific sections within an operating environment has escalated the necessity of new manufacturing routes. Inertia Friction Welding (IFW) stands out as a promising technology above conventional fusion welding techniques as it is capable of creating a joint between either similar or dissimilar materials which exhibits the parent metal strength without the necessity of filler metal and thus avoiding weight penalties. It is considered a solid-state joining technique as no bulk melting takes place at the interfaces to be welded, instead coalescence is obtained through the combined effects of pressure and relative motion of the mating workpieces to cause heating through friction and consequently plastic deformation with the purpose of forming enough primary atomic-level bonds (Messler, 1942).

The IFW machine (Figure 1) is designed to convert kinetic energy into thermal energy at the interfaces to be welded through friction when one stationary workpiece and one rotary workpiece are brought into contact. The flywheel, which is coupled to the rotary workpiece, is accelerated to a predetermined initial speed (*N* rpm) by a drive motor, as illustrated in stage *a)* of Figure 2, thus storing a specific amount of kinetic energy into it (Kearns, 1980). The welding process starts at stage *b)* when the two sections to be joined are brought into contact by an axial force (*F*), which is applied through the stationary workpiece while the rotating power is simultaneously cut off. The frictional heating between the faying surfaces causes the flywheel to decelerate (transition of stage *b* to *c*) by dissipating its kinetic energy as thermal energy and thus resulting in an increase in the temperature of the workpieces around the interface. Once the forging temperature is reached, the softened material plastically deforms until it is expelled around the joint generating the characteristic "flash" and "upset" of the IFW process. The axial load is maintained for the initial part of the cooling period after the flywheel comes to rest at stage *c)* to consolidate the weld (Bennett, 2007b).

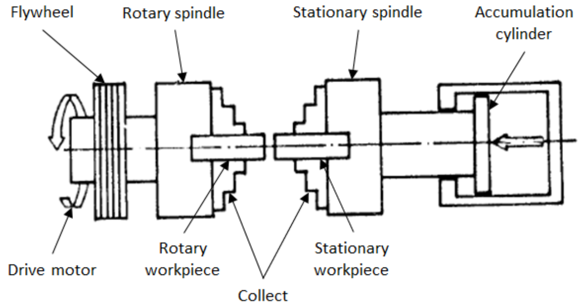

Figure 1. Schematic diagram of a typical inertia friction welding machine (Kearns, 1980).

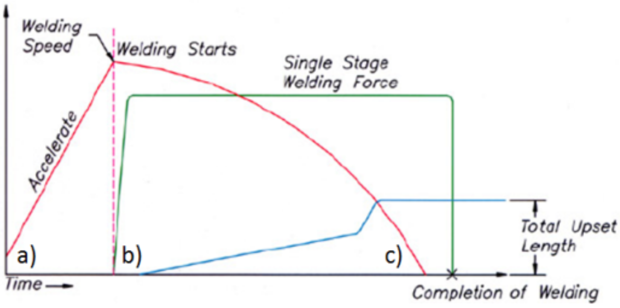

Figure 2. Stages of the IFW process (Bennett, 2007b).

In terms of thermo-mechanical cycles, the process can be separated into two general stages: a welding stage or heating stage and a cooling stage. The welding stage is characterized by an instantaneous discharge of kinetic energy as a heat flux at the faying surfaces and high strain rates. During the early period of welding, contact between workpieces is made over the asperities of the surfaces and hence the real contact area is smaller than the apparent contact area. In this period a sliding condition is fulfilled in which asperities are deformed by frictional shear stresses following a Coulombic friction law ($\tau_{fric} = \mu p$) and therefore heat is generated through friction. However during the last period of welding, initiated once the real contact area equals the apparent contact area as a result of plastic flow of material, frictional shear stresses become independent of normal pressure (p) and the sliding condition is now replaced by a sticking condition. Here, frictional shear stress takes the value of the shear yield stress of the workpiece material ($\tau_{fric} = \tau_y$) and heat is generated by plastic deformation rather than friction (Grant, 2009; Maalekian, 2007). Plastic strain is confined to a narrow region in the vicinity of the weld line, reaching the highest values at the weld line (WL) as shown schematically in Figure 3a. Next to the WL is the fully plasticized zone (FPZ), where a combination of high peak temperature, plastic strain and strain rates cause grain refinement due to dynamic recrystallization. Larger grains compared to the parent metal grain size are found in the partly deformed zone (PDZ) due to grain growth caused by high temperature and lower strain and strain rates compared to the FPZ. Away from the weld line, but inside the heat affected zone (HAZ) an undeformed zone (UZ) is located where material is subjected to thermal effects but plastic deformation does not occur. In this zone, depending on the peak temperature, material may experience some grain growth and also particle growth or dissolution, if these exist in the pre-weld microstructure (Phase A), leading to the formation of a new phase (Phase B).

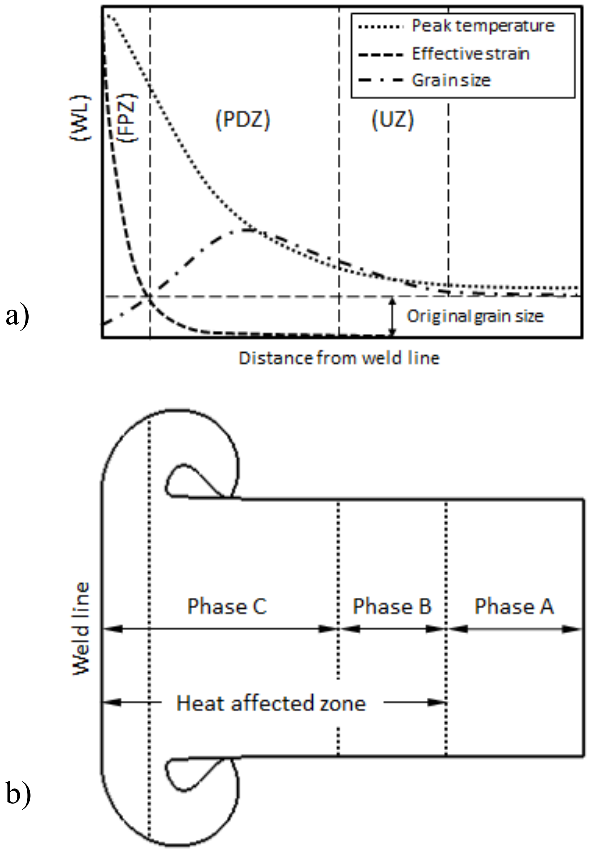

Figure 3. a) Schematic diagram of the typical thermo-mechanical behavior and b) generated metallurgical zones in IFW welds.

The cooling stage however is characterized by low strain rates and is dominated by elastic thermal expansion/contraction. Typical temperatures in the FPZ and the PDZ exceed the transformation temperature of some materials during the welding stage, leading to the formation of a different phase on cooling (Phase C).

Numerical approximations to the physics governing the process can allow assessment of the structural integrity of the inertia friction welded components during service, however, only a very limited number of works have been published throughout more than half a century of existence of IFW. The earliest scientific studies on friction welding were released during the late 1950’s in the former U.S.S.R. Rykalin et al. (Rykalin, 1959) published the first analytical solution to the thermal aspects of friction welding, and Vill (Vill, 1959) studied the process by characterizing the heating period in three friction stages: dry friction, rapid increase in seized region, and high temperature with steady state.

Wang and Nagappan (Wang, 1970) established the numerical analysis concerning the transient temperature distribution in IFW of steels using a finite difference approach for the calculation of the thermal behavior, considering convection heat losses through the periphery of the workpiece but neglecting radiation losses. The possibility of melting at the interface was considered and investigated by comparing the numerical solution of temperature at every node with the melting temperature of the material, however it was concluded that no melting occurred. The computed temperatures were in good agreement with the measured values at the end of the welding cycle, approximately 2.5 – 12.5 % overestimated, although at the early welding stage, the measured temperatures were considerably lower, approximately 50% the computed temperatures, due to the slow response of the air pressure build-up in the cylinder.

The first attempt to develop a fully coupled thermo-mechanical model for the IFW process was presented by Moal and Massoni (Moal, 1995) with the FE code INWELD. The code included an adaptive remeshing procedure and used axisymmetric elements to mesh the components, each was node defined with a three-component velocity vector to account for the torsional effects. The predicted rotational velocity was in very good agreement with experimental measurements. However, the evolution of the axial shortening was overestimated by the model at the end of the welding process, which was attributed to an inaccurate determination of the rheological, friction and thermal coefficients when the temperature reaches a value near the melting point of the material. Using a similar approach to model the torsional effects, Lee et al. (Lee, 2001) extended the DEFORM-2D code to a

2.5D model with the development of a special axisymmetric element. The capability of the FE model to predict the slowdown of the flywheel was satisfactorily validated against analytical solutions of energy decay and shear stress used to represent the torsional behaviour. Additionally, a good agreement was found between the predicted and measured upset.

The numerical analysis to predict the evolution of residual stresses during IFW has received even less attention in the past and a very limited number of studies exist in the literature. Wang et al. (Wang, 2005) developed a representative coupled thermo-mechanical FE model based on the energy input method described by Balasubramanian et al. (Balasubramanian, 1999) to simulate the inertia welding of RR1000 nickel-base superalloy tubes. The heat input and upset data were obtained experimentally and defined as boundary conditions in the FE model, thus neglecting friction at the interfaces of the weld and the torsional deformation. The peak temperatures experienced along the mid-wall line in an inertia welding trial were inferred by comparing the distribution of γ' particles with curves of γ' volume fractions as a function of temperature, generated by heating "matchstick-like" samples using an electro-thermal mechanical tester (ETMT) machine. The thermal fields predicted by the FE model satisfactorily matched the values inferred from thermal simulations with discrepancies ranging from 70–100 °C. In the same way, the FE model was capable of predicting the final residual stress with a good level of agreement, although slightly overestimated, with the experimental results obtained by neutron diffraction measurements. This study demonstrated the dependency of the size of the HAZ on the initial *rpm* of the flywheel, being smaller for higher *rpm* as most of the heat is generated early during the welding process expelling much of the hot material into the flash. This model was improved by Grant et al. (Grant, 2009) by including a better material database, a more representative heating model, and by assuming an elastic-plastic material model to predict residual stresses. In this study, the thermal history predicted by the FE model were mimicked in "matchstick-like" samples of RR1000 using an ETMT machine. The peak temperatures experienced in the welding trials and in the matchstick samples were inferred from the resultant volume fractions following the same procedure described by (Wang, 2005). The FE model prediction slightly underestimated by about 20°C the inferred peak temperatures in the inertia welding trial. The predicted residual stress field in the as-machined condition was in very good agreement with the experimental measurements in the hoop and radial directions. However, significantly smaller predicted values were found in the axial direction, partly attributed to an inappropriate tooling arrangement defined in the model. This study demonstrated the dependency on the thermal behavior to the weld pressure but concluded that the higher residual stresses near the weld line which lie in the hoop direction are independent of the welding pressure as these are limited by the low yield strength values of the alloy at high temperatures.

Bennett et al. (Bennett, 2007b) developed a modelling tool based on DEFORM-2D to simulate both a mono-material weld of Inconel 718 and a dual-material weld of Inconel 718 to AerMet 100. In this study the importance of volumetric changes associated with phase transformations on the prediction of post-weld residual stresses was highlighted by a reduction in the von Mises stress predicted in the HAZ. This work was advanced further (Bennett, 2013) using experimental data to compare the predictions of the FE model to the residual stresses and the width of the region in which martensite transformed to austenite during the welding stage; both predictions were in good agreement with experimental data. However, a further development of the material model was suggested to improve the residual stress predictions.

It is to be noted that only the last two pieces of work, (Bennett, 2007b) and (Bennett, 2013), included stresses associated to volumetric changes occurring during phase transformations in the material within the HAZ. Therefore in this study, transformation induced plastic strains have been taken into account with an improved FE model capable of predicting the polymorphic transformations in a CrMoV steel. The evolution of the total strain due to microstructural changes and the interrelationship of multiple phases, as well as due to different processing parameters such as the die geometry, clamping history and cooling rates, has been studied in order to define the most favorable state of stress in the as-welded condition.

2 Materials and methods

The variation in mechanical properties in a mono-material weld between cylinders of CrMoV steel (Figure 4) resulting from the complex thermo-mechanical field induced by the IFW process has been studied through the material characterization in a thin cross-weld slice section of the HAZ. This provided both an understanding of the effects of the process on the material and also information to guide the development of an improved material database, which has been used for the FE modelling.

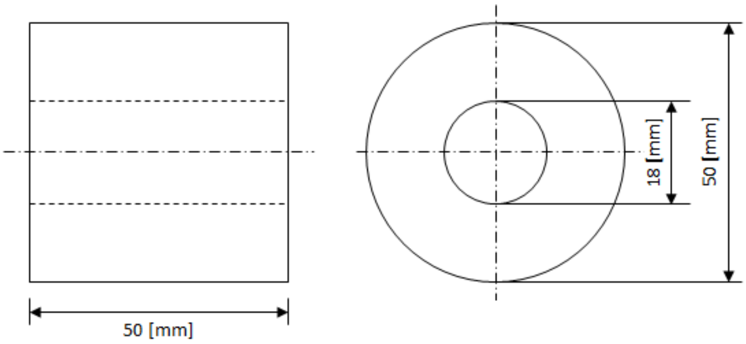

Figure 4. Geometry of the workpieces.

2.1 Thermo-mechanical evolution across an inertia friction weld of a CrMoV steel

During the welding stage of a CrMoV steel, part of the body-centered-cubic (bcc) tempered martensite in the base metal reaches temperatures above A_{c1} (~834°C) (Bennett, 2013) within the heat affected zone (HAZ) and thus transforms to face-centered-cubic (fcc) austenite. The bcc structure is not as tightly packed as the fcc structure and thus upon heating the microstructure experiences a negative (decrease) volumetric change. During the cooling stage however, fcc austenite exposed to high cooling rates transforms back to quenched martensite at temperatures below A_{r3} (~300°C) (Bennett, 2013), resulting in a highly distorted bcc lattice due to the presence of carbon atoms that remain in solution. This structure is known as body-centered-tetragonal (bct) lattice, which in turn results in a positive (increase) volumetric change (Bennett, 2007b). The thermo-mechanical evolution within the HAZ was investigated by means of optical microscopy and a microhardness test. Figure 5 is a sequence of micrographs combined as one composite image showing the three characteristic zones within the HAZ revealed in the microhardness profile presented in Figure 6. As explained previously in Figure 3a, temperatures in the UZ which is located in the region adjacent to the base metal, between ~ 3 to 5 mm away from the weld line, remain below the A_{c1} yet reach sufficiently high levels such as to promote coarsening in the precipitates (Moat, 2008), leading to the formation of over-tempered martensite (OTM) which consequently leads to the hardness trough shown in the microhardness profile at ~ 4.8 mm. The PDZ (~ 0.5 to 3 mm) is comprised of quenched martensite (QM) formed due to rapid cooling rates, which can be inferred from the abrupt change in flow direction (Lippold, 1984) as revealed in Figure 5, where material flow tends to align with the centre line of the shaft away from the weld line. QM is responsible for the hard region located between 0 to 3 mm away from the weld in the microhardness profile. However, the FPZ (0 to ~ 0.5 mm) is identified as QM further hardened as a result of the grain size reduction due to dynamic recrystallization described in Figure 3a.

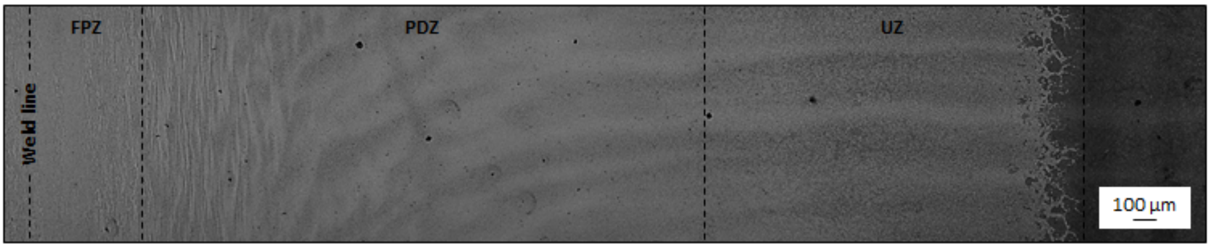

Figure 5. Sequence of micrographs showing the characteristic regions comprising the HAZ generated by IFW in the CrMoV steel (Bennett, 2014).

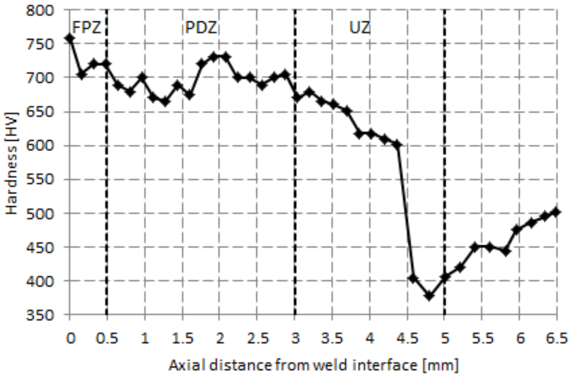

Figure 6. Microhardness profile across the HAZ of a CrMoV steel weld trial (Reproduced from (Mohammed, 2011)).

2.2 Representation of the IFW process in FE modelling

In this study, the FE analysis was split into two models to represent different parts of the welding process, a welding model and a cooling model. The welding model extends in time from the beginning of the process to the complete deceleration of the flywheel, whereas the cooling model consists of an initial period of 45 s with the axial force (F) applied and a second period of 3600 s with no axial force to simulate the final cooling period after the welded component has been removed from the welding machine. The final nodal displacements, nodal temperatures and volume fractions calculated in the welding model were exported to the cooling model as the initial conditions.

2.2.1 Process parameters

Using the pre-set parameters for welding described in Table 1, the torsional motion of the rotary die was defined in the FE model using a movement control based on kinetic energy (E_k), moment of inertia (I), and an efficiency parameter to take into consideration other factors of the system that inherently contribute to the energy losses.

Table 1. Initial process parameters for welding

Input	Value
Flywheel moment of inertia, *(I)*	30973 [N-mm-s^2]
Energy, *(E_k)*	232780 [J]
Axial force, *(F)*	117834 [N]

The total amount of kinetic energy (E_k) available to generate heat was calculated using:

$$E_k = \frac{1}{2} \cdot I \cdot \omega^2 \tag{1}$$

where the value of moment of inertia (I) and the nominal angular velocity (ω) were taken from the specifications of the inertia friction welding machine. In addition, the axial load during welding was introduced in DEFORM as a constant force (F) derived from the welding parameters:

$$F = PSIg \cdot A_{gauge} \tag{2}$$

where $PSIg$ is the pressure in the hydraulic cylinder acting on the gauge area A_{gauge}.

2.2.2 Friction law

Based on the work described by Balasubramanian et al. (Balasubramanian, 1999), the slowdown of the flywheel was computed in terms of available kinetic energy. For a given time-step (n) the FE software updates the available kinetic energy after the losses due to friction as follows:

$${E_k}^{n+1} - {E_k}^{n} = -\Delta t \cdot \omega \cdot \bar{T} \tag{3}$$

where ${E_k}^{n+1}$ and ${E_k}^{n}$ are the rotational kinetic energies at the next and current time steps, ω the angular velocity, Δt the time period and $\bar{T}$ the generated torque. The torque is computed by integrating the cross product of surface traction (f_s) and the radial distance (r) over the contact area (A_c) as expressed in Equation (4).

$$\bar{T} = \int_{A_c} f_s r dA_c \tag{4}$$

If the surface traction is defined by a classic Coulomb friction model throughout the process,

$$f_s = \mu p \tag{5}$$

where μ is the friction coefficient and p is the normal pressure, the apparent coefficient of friction can be defined as detailed by Bennett et al. (Bennett, 2007b):

$$\mu^n = \frac{\left({E_k}^{n+1} - {E_k}^{n}\right)}{-\omega \cdot \Delta t \cdot p \cdot \left[{}^{2\pi}/_{3} \cdot (r_o^3 - r_i^3)\right]} \tag{6}$$

Here, the numerator represents the energy loss ($-\Delta E$) as a function of the angular velocity (ω) obtained from the rpm measured during the inertia welding trial, Δt is the time period, p is the normal pressure, r_o the outer radius and r_i the inner radius of the contact at the weld interface. The apparent coefficient of friction defines the average contact condition over the entire interface area for a given time period assuming contact is maintained across the interface with constant values of contact pressure (p) and interface area (r_o, r_i).

2.2.3 Material behaviour

It was assumed that during welding the crystals remain randomly oriented so that isotropy is preserved and that as plastic deformation increases, the yield stress and yield locus continuously expands according to the isotropic hardening rule. For isotropic materials, plastic yielding is only dependant on the magnitude of the three principal stresses and not on their directions (Kobayashi, 1989), hence by using the von Mises yield criterion, flow occurs if the effective stress is equal to or greater than the flow stress of the material.

$$\frac{1}{\sqrt{2}}\sqrt{(\sigma_1 - \sigma_2)^2 + (\sigma_2 - \sigma_3)^2 + (\sigma_3 - \sigma_1)^2} \geq \bar{\sigma} \tag{7}$$

In this study, the material was assumed to behave rigid-viscoplastic during the welding stage, when elastic strains are negligible in comparison to the plastic strains, whereas upon cooling the material model was switched to elastic-plastic in order to capture the evolution of the residual stress field. In order to improve convergence in the rigid-viscoplastic FE model, a limiting strain rate is defined to calculate a consistent stress in rigid, or nearly rigid regions of the workpiece showing near zero deformation rates. Therefore at values of effective strain rate ($\dot{\bar{\varepsilon}}$) below the limiting strain rate ($\dot{\bar{\varepsilon}}_0$), the material was considered rigid and the stress-strain rate relationship is defined by the viscoplastic constitutive equation:

$$\dot{\varepsilon}_{ij} = \frac{2}{3}\frac{\dot{\bar{\varepsilon}}_0}{\bar{\sigma}_0}\sigma'_{ij} \quad , \quad \text{with } \bar{\sigma}_0 = \bar{\sigma}(\bar{\varepsilon}, \dot{\bar{\varepsilon}}_0) \quad , \quad \text{for } \dot{\bar{\varepsilon}} \leq \dot{\bar{\varepsilon}}_0 \tag{8}$$

in which $\dot{\varepsilon}_{ij}$ represents the deviatoric strain rate, $\dot{\bar{\varepsilon}}_0$ the effective strain rate, $\bar{\sigma}_0$ the effective stress and σ'_{ij} the deviatoric stress. For the plastic regions however, the Levy-von Mises flow rule can be used to relate the stress tensor to the strain rate tensor (SFTC, 2011).

2.2.4 Deformation analysis

The mechanical formulation employed for the calculation of metal flow is based on the minimum work-rate principle (Kobayashi, 1989), in which the best approximation of the actual velocity distribution is at the lowest work rate since the principle states that *'the material should always flow in the path of least resistance'* (SFTC, 2011). Body forces are balanced with surface tractions according to the work rate function (π):

$$\pi = \int_V \bar{\sigma}\dot{\bar{\varepsilon}}\,dV - \int_S F_i u_i\,dS \tag{9}$$

where $\bar{\sigma}$ represents the effective stress, $\dot{\bar{\varepsilon}}$ the effective strain rate, *u* the velocity, and *F* is the surface traction. Equation (9) has to be minimized for the case when the variation in the function is stationary in order to achieve the minimum work rate as follows:

$$\delta\pi = \int_V \bar{\sigma}\delta\dot{\bar{\varepsilon}}\,dV - \int_S F_i \delta u_i\,dS + K\int_V \dot{\varepsilon}_V \delta\dot{\varepsilon}_V\,dV = 0 \tag{10}$$

The third term in the right-hand side is added to maintain incompressibility in the solution, in which $\dot{\varepsilon}_V$ is the volumetric strain rate and *K* is a penalty constant.

2.2.5 Thermal analysis

The dissipation of energy due to frictional traction generates a heat flux at the faying surfaces as expressed in Equation (11) (Mohammed, 2011), which in turn leads to temperature increase. Here, the product of the coefficient of friction μ and the normal pressure *p* represents the frictional traction, *r* is the radial distance and ω is the rotational velocity.

$$q_f = 2\pi \cdot r \cdot \mu \cdot p \cdot \omega \tag{11}$$

The thermal formulation is based on an energy balance of heat generated by friction and plastic deformation, with the heat absorbed and transferred by the material (Kobayashi, 1989). The first term in the left-hand side of Equation (12) represents the contribution of heat generated by friction at the faying surfaces, and the second term is the heat generated by plastic deformation inside the workpiece.

$$\begin{aligned}\int_S q_f \cdot dS + \int_V (\bar{\sigma} \cdot \dot{\bar{\varepsilon}}) dV \\ = \int_V \rho \cdot C_p \cdot \frac{dT}{dt} \cdot dT \cdot dV \\ + \int_V K_c \cdot T \cdot dT \cdot dV \\ + \int_S h_c \cdot (T_e - T_s) \cdot dS \\ + \int_S \sigma \cdot \xi \cdot \left({T_e}^4 - {T_s}^4\right) \cdot dS\end{aligned} \tag{12}$$

The right-hand side expresses in terms one to four respectively, the heat absorbed by the material due to its heat capacity (*Cp*), the heat transferred by conduction, the heat transferred by convection, and the heat transferred by radiation. Heat transfer across the workpiece-die contact interface has been neglected in this study. In Equation (12), V represents the volume of the deforming body (workpiece), ρ the material density, K_c the thermal conductivity, h_c the convection coefficient, T_e and T_s are the environment and surface temperatures, respectively, σ the Stefan-Boltzmann constant and ξ the emissivity. The integration limits are selected according to the surface on which heat is being transferred.

2.2.6 Material properties

During IFW of CrMoV steel, the base metal within the HAZ experiences a polymorphic transformation from the parent phase of tempered martensite into two child phases, austenite and quenched martensite as detailed in section 2.1. Therefore, the current material database for CrMoV steel (Bennett, 2007b) has been improved in this study in order to include in the FE model the material behaviour and interrelationship of each of the present phases in the HAZ. Tempered martensite exists at low temperatures as the base metal in the pre-weld condition. The original material database (Bennett, 2007b) was introduced unaltered during the welding stage as it covers a wide range of strains, strain rates and temperatures. At the onset of cooling however, strain rates are significantly lower and thus it is possible to simplify the FE model by assuming a constant strain rate and the plastic behavior is expressed according to the power law hardening rule:

$$\bar{\sigma} = \sigma_y + K{\varepsilon_p}^n \tag{13}$$

where $\bar{\sigma}$ is the flow stress at the corresponding plastic strain ε_p and σ_y is the yield strength. The strength coefficient (K=733.63) and the strain-hardening exponent (n=0.3915) were determined from experimental data using a least squares fit. As shown in Figure 7, tempered martensite destabilizes at above 600°C, as can be inferred from the evolution of the yield strength at different temperatures captured by the hot compression testing of CrMoV steels (Bennett, 2007b), and starts to transform to austenite at approximately 834°C (A_{c1}) (Bennett, 2013). Upon cooling however, austenite exists at lower temperatures compared to A_{c1} (Bennett, 2013) and therefore the high temperature values (beyond A_{c1}) were linearly extrapolated as illustrated in Figure 7 in order to cover the range of temperatures where austenite remains unaltered upon cooling.

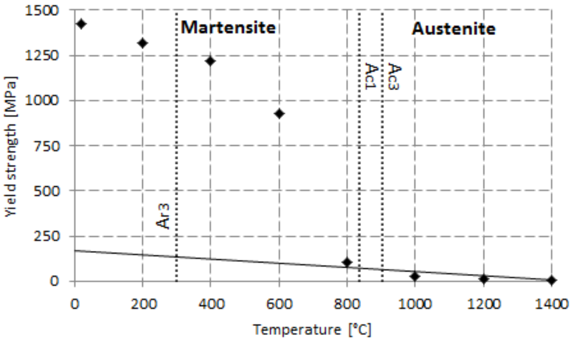

Figure 7. Levels of yield strength taken from the hot compression testing in CrMoV steel carried out by Bennett et al. (Bennett, 2007b) at different temperatures.

The power law was used for the austenitic phase in a similar manner as for tempered martensite using the stress value extrapolated to room temperature as the austenite yield strength. The yield strength (σ_y) of quenched martensite was correlated to the average hardness (*HV*) recorded by the microhardness test shown in Figure 6 using Tabor's relationship (Tabor, 1951):

$$HV = 2.9\bar{\sigma}_{(0.08)} \tag{14}$$

where *HV* is the Vickers hardness number and $\bar{\sigma}_{(0.08)}$ is the flow stress at an engineering plastic strain (ε_p) of 0.08. The accuracy of Tabor's relationship was tested by comparing the correlated value of flow stress to the Vickers hardness level in the base metal (tempered martensite) according to the microhardness profile in Figure 6, with the flow stress obtained experimentally by the hot compression test. This relationship provided an excellent approximation (<0.08% error) to the yield stress in the tempered martensite. The power law was employed to represent the strain hardening in the plastic region, and a reduction in yield strength due to temperature similar to the tempered martensite phase was assumed to cover the range of temperatures in which the quenched martensite phase exists.

2.2.7 Phase transformations

Transformation induced strains are crucial in the analysis of metal working processes such as IFW as the associated volumetric changes modify the residual stress field and will certainly affect the final dimensions after processing. Therefore, the accuracy of the FE model depends on an appropriate representation, at an affordable computational cost, of the metallurgical evolution across the joint. Four simulations were run in this study with increasing complexity of material model as summarized in Table 2.

Table 2. Simulations to examine the effects of the inclusion of multiple phases in the FE model

Simulation	Tempered martensite	Austenite	Quenched martensite
A	✓	-	-
B	✓	✓*	-
C	✓	✓	-
D	✓	✓	✓

*Austenite phase defined with identical material properties as tempered martensite.

Simulation A is a single phase model which included just the material properties of the original tempered martensite parent metal; this model neglected transformation strains. Simulation B included tempered martensite at low temperatures and austenite at high temperatures using the original parent metal properties for both phases over the entire range of temperatures; this simulation included transformation strains but no details of different properties between phases. Simulation C is a two-phase model similar to B with additional properties of the austenite phase at lower temperatures on cooling as described in section 3.6. Simulation D was defined as a three-phase model similar to C but allowing the transformation of austenite to an additional phase on cooling, quenched martensite. The last three simulations highlighted the interrelationships and effects of transformation strains generated throughout the transformation paths schematically illustrated in Figure 8.

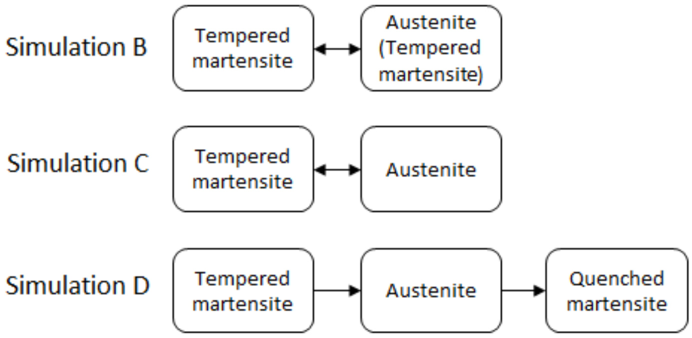

Figure 8. Transformation paths for each simulation.

The nodal temperatures were analyzed by the DEFORM-HT add-on according to the energy balance in Equation (12) to simulate additional effects in the material including phase volume fraction, distortion and residual stresses. DEFORM-HT is coded with different kinetics models to define the conditions and manner in which one phase is transformed into another (SFTC, 2011). The kinetics of transformation upon heating was included using a diffusion-type function as shown in Equation (15) to calculate the volume fraction of tempered martensite transformed to austenite:

$$\xi_J = 1 - \exp\left\{A\left(\frac{T - T_{As}}{T_{Ae} - T_{As}}\right)^D\right\} \tag{15}$$

where ξ_J is the volume fraction of the austenite phase, T is the average element temperature, T_{As} is the transformation start temperature, T_{Ae} is the transformation end temperature, and A and D are constants. A, D, T_{As}, and T_{Ae} were obtained experimentally for CrMoV steels in a previous study (Bennett, 2013). A simplified form of the Magee's equation was employed for representing the kinetics of transformation from austenite to martensite as follows:

$$\xi_M = 1 - e^{(\psi_1 T + \psi_4)} \tag{16}$$

where, ξ_M is the volume fraction of martensite, T is the average element temperature, and ψ_1 and ψ_4 are constants determined in a previous study (Bennett, 2007b). Volumetric strains generated due to phase transformations are calculated in the FE model using:

$$\dot{\varepsilon}^{Tr}{}_{IJ} = \sum \beta_{IJ}\dot{\xi}_J\delta_{ij} \tag{17}$$

where $\dot{\varepsilon}^{Tr}{}_{IJ}$ is the transformation strain rate from phase I to phase J, β_{IJ} is the fractional length change, $\dot{\xi}_J$ is the transformation volume fraction rate, and δ_{ij} is the Kronecker delta. The fractional length parameter has been defined in the FE model according to a previous experimental analysis in CrMoV steels (Bennett, 2007a).

2.2.8 Coupled thermo-mechanical analysis

In IFW, the energy for welding is produced by direct conversion of mechanical energy into thermal energy. Frictional heat flux at the faying surfaces is transferred to the far-field of the workpieces, thus generating a plastic zone which extends from the weld line to a distance *h* where the temperature remains at a minimum necessary level for compressive yielding at the local forging stress as illustrated in Figure 9. Material within this zone is progressively deformed by the rigid sections as these move towards the interface of the weld by the compressive load (*F*) (Rich, 1971). The distance *h* at the end of the welding stage corresponds to the fully plasticized and partly deformed zones detailed in Figure 3.

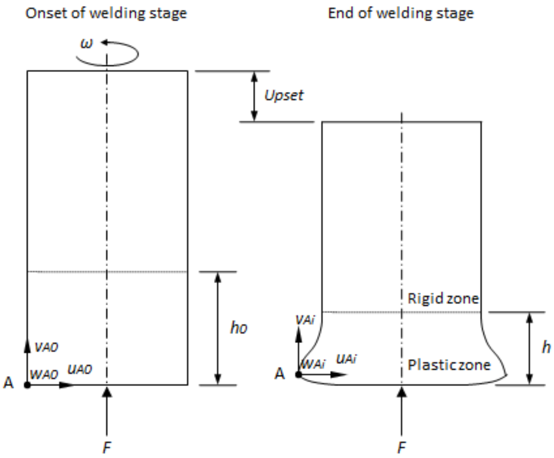

Figure 9. Appearance of the pre-weld workpiece (left) and at the end of the welding stage (right). Based on (Rich, 1971).

It is crucial in the analysis of IFW to consider the strong coupling between the deformation and heat transfer phenomena. During the welding stage, the displacement of a given point *A*, located at the outer diameter (OD) of the workpieces interface before welding, as illustrated in Figure 9, is strongly dependent on the local temperature as the flow stress of the material represented by *A* is a function of the effective strain, effective strain rate and temperature. Therefore, instead of a sequentially mechanical and thermal formulation, the FE model updates for each time step the nodal velocity vector (*u*, *v*, and *w* components in the radial (*r*), axial (z) and hoop (θ) directions respectively) satisfying the minimum work-rate principle, from which the key mechanical variables are calculated. Subsequently, in the same time step the nodal temperatures satisfying the energy balance, considering the previous temperature state, are calculated. At the end of each time step, the total strains are accumulated in the welded parts according to the material model, rigid-viscoplastic at the onset of welding or elastic-plastic upon cooling:

$$\varepsilon_{total} = \varepsilon_e + \varepsilon_p + \varepsilon_T + {\varepsilon^{Tr}}_{IJ} \tag{18}$$

where ε_e and ε_p are respectively the elastic and plastic strain components associated with mechanical deformation, ε_T is the thermal strain resulting from temperature changes in the material, and ${\varepsilon^{Tr}}_{IJ}$ are inelastic strains due to phase transformation.

2.2.9 Geometrical representation and boundary conditions

Due to symmetry in the geometry and material of the workpieces, only the rotary die and the rotatory workpiece were included in the analysis and the stationary workpiece and the stationary die were replaced by a rigid plane as shown in Figure 10. A sticking condition was defined between the "L-shaped" die and the rotary workpiece as a velocity boundary condition to ensure the rotational speed is transmitted to the rotary workpiece. The internal diameter (ID) of the die was defined to match the OD of the workpiece, however, heat transfer was neglected at die-workpiece interface. An inter-object contact condition in the outer nodes of the rotary workpiece was defined for the case of any self-contact during the simulation. The frictional traction (f_s) was defined by a contact boundary condition at the interface of the rotary workpiece and the rigid plane using the representative technique described in section 2.2.2. The special axisymmetric element developed by Lee et al. (Lee, 2001) was used to mesh the workpiece in order to include torsional effects. Considering that the mesh is not severely distorted at the onset of welding by the low pressure IFW process studied in this work, an adaptive remeshing procedure was not included in order to avoid an excessive computation time and interpolation errors.

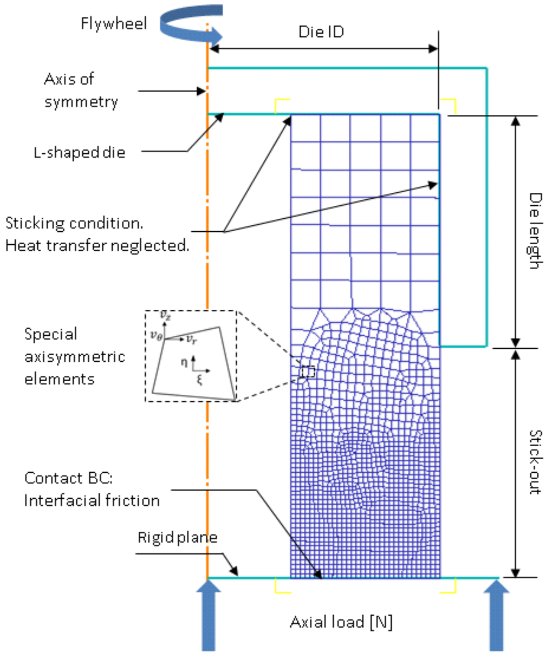

Figure 10. Welding model set-up and boundary conditions.

3 Results and discussion

The FE model presented in this study can provide a reliable insight into the effects of the process parameters on the complex thermo-mechanical field developed within the HAZ in order to predict the distribution of mechanical properties across the joint and the final state of stress in the component. The objective of this study is to test the sensitivity of the residual stress field predicted by the FE model to the microstructural phases taken into consideration, the approaches taken to define the material database of each of these phases from the parent material and to different processing parameters such as the die geometry, clamping history, and cooling rates.

3.1 Evolution of residual stresses during IFW

This section introduces the typical state of stress induced by the IFW process in the component throughout the two general thermo-mechanical cycles: welding and initial and final cooling. Dissimilar stress fields are expected at different radial distances from the centre line given the strong dependency on the distribution of pressure and friction over the weld interface to the radial distance (Wang, 1970). However, the regions of interest are either the ID or OD as failure is prone to occur near these surfaces due to higher residual stresses as seen in Figure 11. Low residual stresses are generated due to plastic deformation during the welding stage given the high temperatures reached in this stage which reduce the yield stresses of the materials being welded. Plastic stresses at the end of the welding stage in the three cylindrical directions (r, z, θ) are majorly compressive. The build-up of residual stresses during the initial cooling period is dominated by thermal strains due to high cooling rates experienced by the material located in regions near the weld line, as explained in the following section, and the constraint imposed by the axial load. Higher peak temperatures are reached at the mean diameter (MD) given that although the rate of heat input is a function of the radial distance and angular velocity, heat losses by convection and radiation to the surrounding environment are negligible, unlike at the ID and OD surfaces. Therefore, lower cooling rates are expected in the MD and consequently lower residual stresses compared to the ID and OD. During the final cooling period, the rate of temperature change has decreased significantly leading to moderate changes in the final residual stress field in the HAZ and a stress reduction beyond the HAZ due to near constant cooling rate (dT/dt) for a prolonged time without the presence of mechanical constraints. The peak value generated near the OD (Figure 11c) during the initial cooling is attributed to the radial constraint imposed by the die as detailed later in section 3.5.1.1.

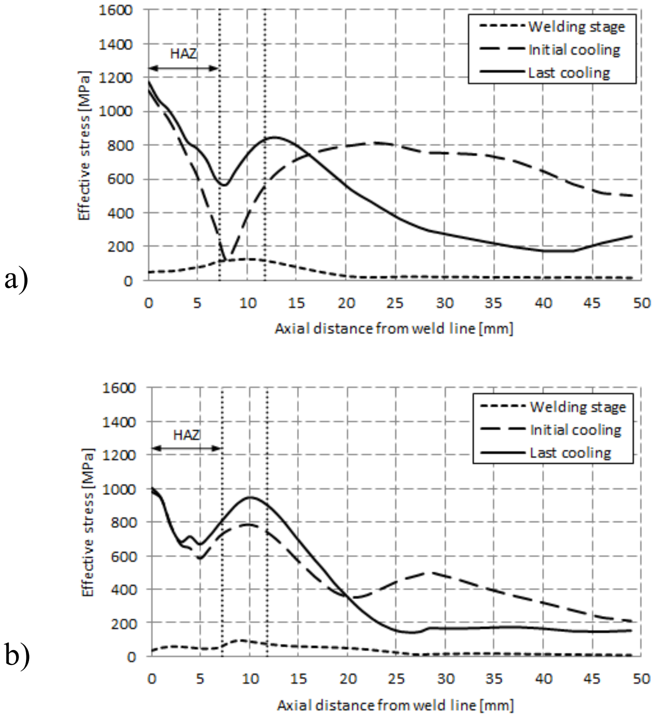

c)

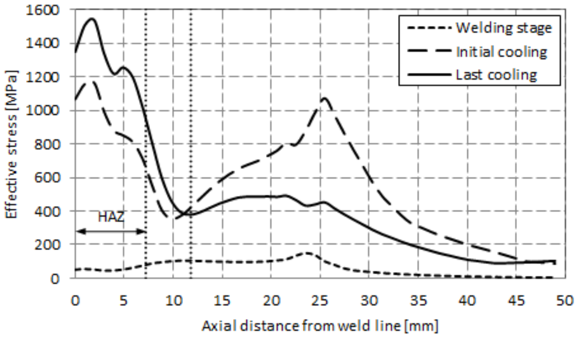

Figure 11. Evolution of the predicted effective stress field by the FE model (simulation A) at three radial distances: a) 1 mm depth from the ID, b) mean diameter, c) 1 mm depth from the OD.

3.2 Strain components associated with heat transfer

During the IFW process, the large temperature gradients developed within the component promote the build-up of residual stresses due to volumetric changes associated to thermal expansion/contraction and phase transformations. This section describes the mechanisms by which heat transfer affects the total strain in the material.

Figure 12 shows the temperature profile reached at the start of the initial cooling period and the linear cooling rate (*dT*/*dt*) between the start and the end of this period along an axial line at a radial location 1 mm from the OD. High temperatures are reached in the vicinity of the weld line (~ 0 to 3 mm) at the end of the welding stage and the early period of time of initial cooling given that heat flux generated by friction is rapidly transferred inwards by conduction with negligible heat losses through convection and radiation as the contacting surfaces are not exposed to the surroundings. Upon cooling however, temperature is additionally influenced by convection and radiation, although conduction remains as the dominant heat transfer mode for the initial cooling period (Mohammed, 2010). Therefore, during the initial cooling period, material away from the weld line (~3 to 24 mm) and the surrounding environment act as a heat sink leading to fast cooling rates (dT/dt) as illustrated by the dashed line in Figure 12. Thermodynamically, the system tends to reach isothermal conditions and thus a thermal boundary is generated at ~ 12 mm from the weld line where the linear rate of change in temperature between the start and the end of the initial cooling period (or the start of the final cooling period) goes from negative to positive. This means that at the end of the initial cooling period, using the start of the initial cooling period as the reference state, the material between the weld line and the thermal boundary is releasing heat and therefore contracting, whereas the opposite occurs outside this region, between the thermal boundary and the die-workpiece interface. The difference in volumetric changes associated with the thermal boundary induces the residual stress trough revealed at approximately 12 mm from the weld line in Figure 11c. Peak temperatures are generated towards the midpoint of the weld interface during the welding stage with cooler temperatures at the ID and OD, leading to the characteristic curved shape of the HAZ, which in turn results in the offset of the thermal boundary and residual stress trough in Figure 11a and b. Therefore, the build-up of residual stresses during the initial cooling period is dominated by thermal strains.

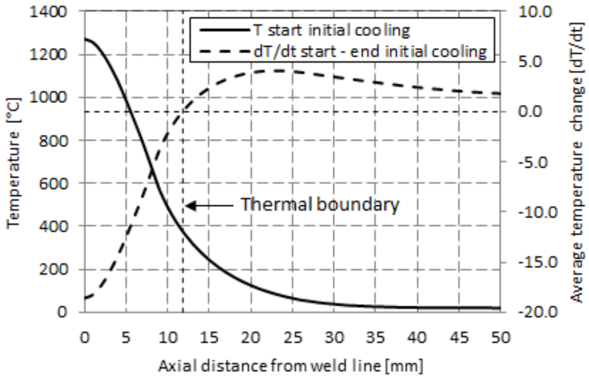

Figure 12. Temperature profile at the start of the initial cooling period along an axial line at a depth of 1mm from the OD.

3.3 *Effects of microstructural changes*

The transformation strain component modifies the total strain only after the temperature within the HAZ is below A_{r3}, which is never reached during the initial cooling period of the IFW of CrMoV steel. During the final cooling period, most of the heat has been dissipated, the rate of change in temperature (dT/dt) reaches near constant values throughout the welded components and the transformation strain within the HAZ becomes the dominant strain component in the generation of residual stresses. This section presents a study on the sensitivity of the final residual stress field predicted by the FE model to the transformation strain and the interrelationship of two or more phases.

3.3.1 *Transformation strain*

Figure 13 presents the effect of the transformation strain on the final residual stress field, in terms of the von Mises effective stress, of a like-to-like weld of CrMoV steel cylinders as predicted by simulation B compared to A at a depth of 1 mm from both the ID and OD. Transformation strains considered for simulation B are responsible for a reduction in approximately 40 to 70% of the effective stresses predicted by A in the vicinity of the weld line as a result of the positive volumetric change experienced in the lattice during the transformation of austenite back to martensite on cooling, as explained in section 2.1. As described in the previous section, residual stresses are generated due to volumetric changes occurring in the vicinity of the weld line during the rapid cooling rates of the initial cooling period and therefore, when transformation strains are neglected as in simulation A, a peak stress is expected at a distance approaching the weld line as shown in Figure 13a. However, in simulation B austenite starts to transform back to martensite from the edge of the HAZ towards the weld line as lower temperatures are reached at early stages of cooling in the far field, and thus the peak value moves away from the weld line to the edge of the HAZ due to the mismatch between the mechanical properties of the austenite and martensite phases.

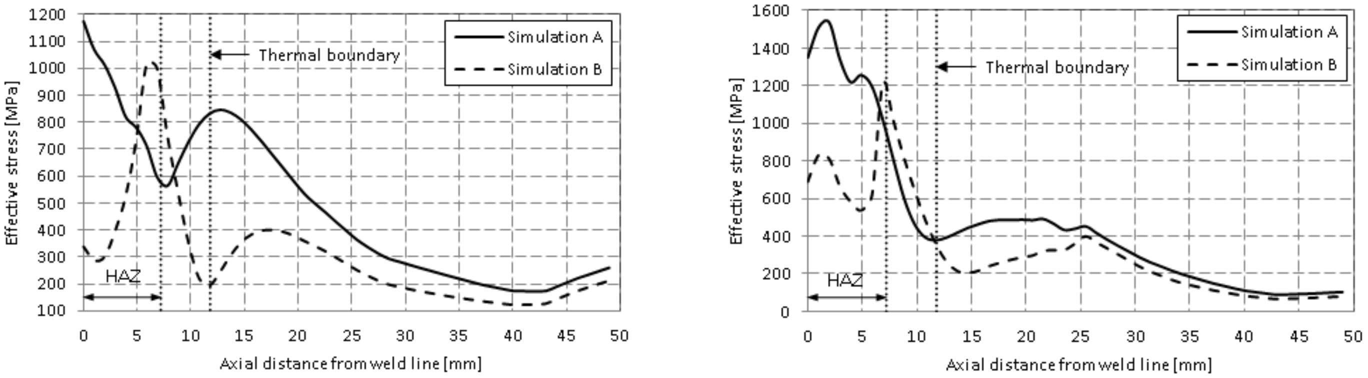

a) b)

Figure 13. Effect of the transformation strain component on the build-up of residual stresses at 1 mm depth from both the a) ID and b) OD.

3.3.2 *Inclusion of multiple phases*

The interrelationship of different thermo-mechanical properties that define each of the phases in the material further influences the evolution of residual stresses as predicted by simulations C and D when compared to B; the von Mises effective stresses at 1 mm depth from both the OD and ID are provided in Figure 14. In a similar manner as for simulation B, simulations C and D present a stress reduction in the vicinity of the weld line compared to A as described in section 3.3.1. However, as austenite formed during the welding stage and the early stage of the initial cooling period remains unaltered until the end of this period given that temperatures within the HAZ remain above A_{r3} (~300°C) (Bennett, 2013), harder regions (martensite) interact with softer regions (austenite) in simulations C and D at the onset of cooling until the HAZ is fully transformed to martensite and small fractions of austenite (<2.7%), or retained austenite, at the end of the final cooling period. Therefore the interaction of strain components associated to different thermo-mechanical properties further modifies the residual stress field predicted by simulations C and D, leading to higher residual stresses (>12%) at regions approaching the edge of the HAZ. In the vicinity of the weld line the evolution of residual stresses is correspondingly affected (reduced at some extent) to accommodate strain components generated at the edge of the HAZ. The inclusion of the slightly harder quenched martensite phase formed in simulation D compared to the tempered martensite obtained in simulation C induced almost negligible residual stresses as the total strain (Equation (18)) generated after the martensitic phases are formed, tempered in simulation C and quenched in simulation D, is similar given that the transformation strain and thermal strains are identical and that the elastic and plastic strains generated during the welding stage play a minor role in the generation of residual stresses during the cooling stage.

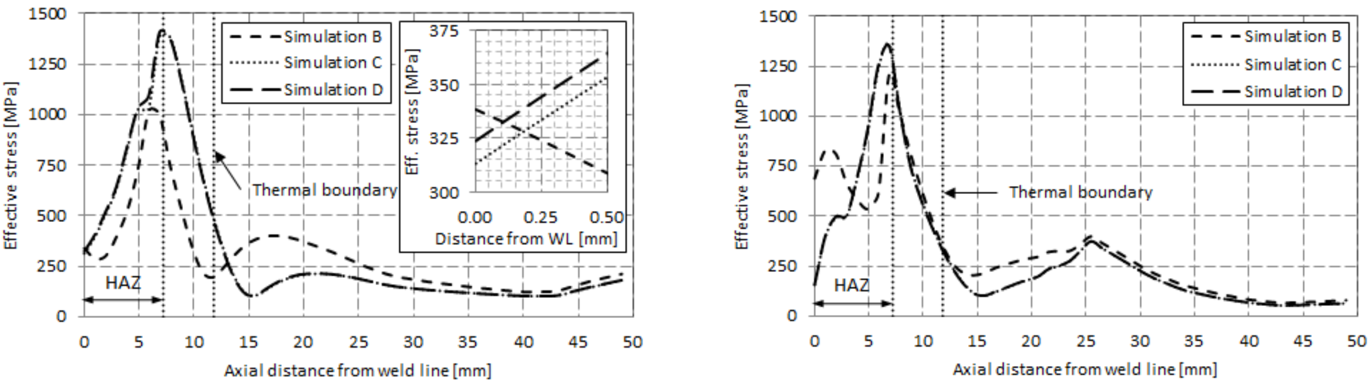

a) b)

Figure 14. Post-weld cooled von Mises stress distribuition at a) 10 mm and b) 24 mm from centre line.

3.4 *Effects of material properties in present phases*

This section assesses the sensitivity of the prediction of residual stresses from the FE model to the approaches taken to define the material database from the parent material. As can be seen in Figure 15, the strength coefficient (K) and the strain-hardening exponent (n) introduced in the power law used to define the plastic behavior of each phase are less significant on the von Mises peak stress compared to the effects induced by the elastic properties due to the almost negligible variation in the flow stress induced by K and n. An approximate variation of 1:1 is observed when increasing the Young's modulus (E) in the quenched martensite phase as the higher the value the lower the total elastic strain component, according to the constitutive equations for isotropic linear elastic materials with thermal strain. Recalling from section 3.3.1 austenite interacts with martensite during the final cooling period, and a higher yield strength (σ_y) results in higher elastic strains recovered after the mechanical constraints are removed. Strain recovery modifies the stress tensor and therefore the increase in von Mises effective stress can be attributed to an increased difference between any two sets of principal stresses induced by elastic stresses.

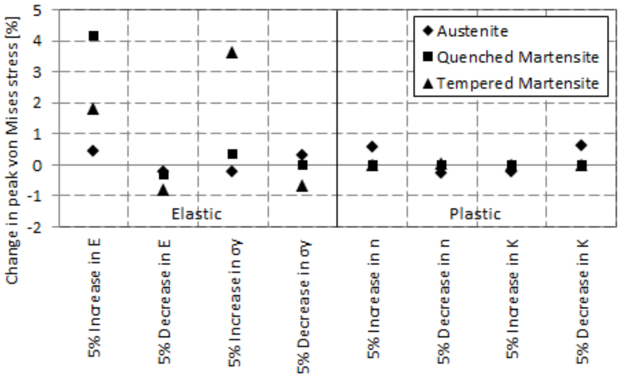

Figure 15. Sensitivity on the peak von Mises stress to small variations in material properties (shown in x-axis) of the present phases (identified by markers).

3.5 *Effects of processing conditions*

Recalling from previous sections, the generation of residual stresses in IFW is dominated by strain components associated with heat transfer, i.e. thermal expansion/contraction and phase transformations. It is possible to control the effects of the heat associated strains in the total strain of the welded component by controlling the processing conditions during IFW and therefore it is important to understand how to promote the most favorable final state of stress.

3.5.1 *Fixtures*

All fixtures employed to perform a weld by the IFW process are designed either to reduce the number of degrees of freedom in the workpiece such that material displacement is constrained, or to set up a physical process in a region of the workpiece. This section studies the effects of the conditions imposed by the die on the evolution of the residual stress field in the welded component.

3.5.1.1 *Component stick-out*

“Stick-out” refers to the axial distance from the weld line to the edge of the L-shaped die in the prior-welding condition as illustrated in Figure 10. Two additional simulations, E and F, with defined stick-out distances of 60% shorter and larger respectively, have been compared with a reference model (simulation A) which has been defined with a stick-out of 25 mm in order to study the effects of the die geometry on the residual stress field. Figure 16 shows the von Mises effective stresses at 1 mm depth from the OD, where a more significant effect is expected due to the proximity to the internal surface of the die. The peaks indicated by points 1, 2, and 3 in the effective stress profile of simulation E, A, and F respectively are formed at an axial distance related to the defined stick-out distance during the initial cooling period as a result of thermal expansion in the positive radial direction, mechanically constrained in the opposite direction by the internal surface of the die. However, this peak vanishes during the final cooling period once the welded component has been removed from the dies due to stress redistribution as shown in Figure 16b, and therefore the stick-out distance is not significant on the final residual stress at the edge of the die. Instead, the sensitivity on the final residual stress to the stick-out distance becomes significant within the HAZ as revealed by an increase in the von Mises effective stress of 2-10% and 15-30% in simulations E and F respectively, compared to A.

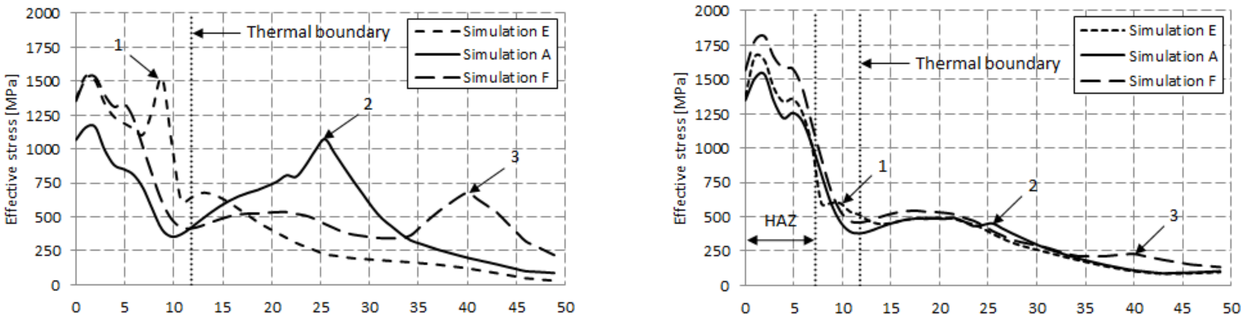

a)

b)

Figure 16. Effects of the die length on the von Mises stress distribution at 1mm depth from the OD after the a) initial and b) final cooling period.

This can be attributed partly to the influence of the stick-out distance on the thermal expansion and contraction in the radial direction experienced during the initial cooling period along the workpieces as explained in section 3.2. The mechanical interaction at the workpiece-die interface also affects the material flow in the radial and hoop directions, leading to 10% increase and decrease in the upsetting distance in simulations E and F respectively, which also modifies the final von Mises effective stress within the HAZ as shown in Figure 16. However, the position of the thermal boundary resulted independent of the stick-out distance, principally because it is strongly linked to the dominant heat transfer mechanism of conduction through the workpiece, but additionally because this FE model neglects heat transfer across the workpiece-die contact interface.

3.5.1.2 Clamping conditions

During the welding stage and initial cooling period, the rotary workpiece is mechanically constrained in the welding machine by a radial load imposed by the rotary die to ensure the transmission of the flywheel's rotational speed. A sticking condition can be defined in the FE model at this boundary as described in section 2.2.9, assuming the workpiece-die arrangement remains concentric throughout the process and a zero offset between surfaces. However, the latter assumption may not be fulfilled if material undergoes excessive thermal contraction. Therefore, in order to identify whether the peak generated at a distance related to the die stick-out is an artificial feature resulting from an over constrained model due to an inappropriate representation the clamping condition, the sticking boundary condition at the die-workpiece interface was replaced by a frictional contact condition. As can be seen in Figure 17, material beyond approximately 15 mm from the weld line is experiencing a positive radial displacement due to thermal expansion. Between 25 to 50 mm radial displacement is ceased by the mechanical constraint in the opposite direction imposed by the inner surface of the die which means material contraction does not occur in this section. Therefore a sticking condition can be used as an appropriate representation of the clamping conditions.

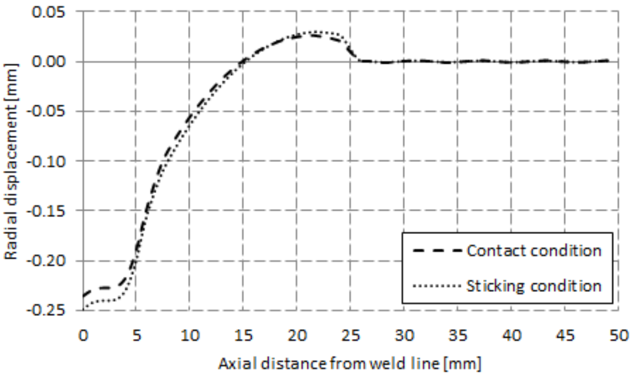

Figure 17. Radial displacement in the outer surface at the end of the initial cooling period.

3.5.1.3 Clamping history

In order to study the effects of the thermo-mechanical cycles, the original initial cooling period (45 s) has been halved and doubled while the total cooling period was maintained to 3645 s. However, a negligible variation was found given that thermal volumetric changes experienced during the early stage of the initial cooling period are the dominant strain component in the build-up of residual stresses when phase transformations are neglected, as explained in section 3.2.

3.5.2 Cooling rates

Cooling rates are governed by the interrelationship of the different heat transfer mechanisms at the surface of the welded component with its surrounding environment. In this FE model however, for simplicity and given that conduction is the dominant heat transfer mechanism upon cooling, two different values of thermal conductivity (a quarter of, and four times the reference value) have been selected as a way to generate the different cooling rate profiles (Figure 18a) used to investigate the effects of the large thermal strains induced from the abrupt thermal variations within the HAZ.

Figure 18b shows the evolution of the von Mises effective stress at a point in the mid-wall of the weld interface during the first 200 s of cooling. As can be seen, the von Mises effective stress is highly sensitive to cooling rates during the initial cooling period (0 - 45 s of cooling) given that thermal strains are proportional to temperature changes in the material, and thus a steeper cooling rate results in larger thermal strains. Therefore, above 90% of the final residual stress is generated during the first 25 s of cooling as can be seen in Figure 18b. The stress reduction at the end of the initial cooling period (45 s) is attributed to the recovery of elastic strain energy in the form of work due to the material stiffness after the axial loading has been removed. The effect of the cooling rate however, is less significant on the evolution of von Mises effective stresses during the final cooling period (45 - 3600 s), when heat transfer is also influenced by convection and radiation. Therefore, the temperature change throughout the welded component approximates constant values as the cooling time approaches the end of the final cooling period, and the build-up of residual stresses due to thermal strains in the material is almost negligible (< 2%). Effective stresses are slightly lower during the final cooling period for the faster cooling rate profile presented in Figure 18a as a steeper cooling rate reaches constant temperature changes at an earlier stage (~ 37% faster).

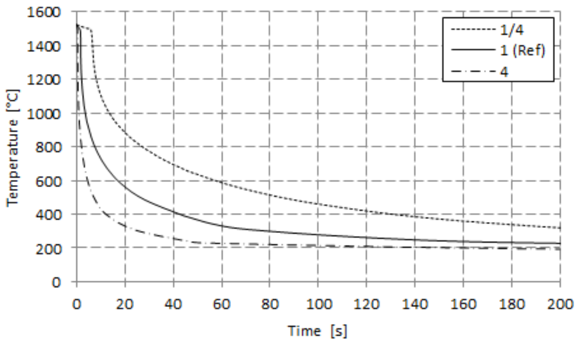

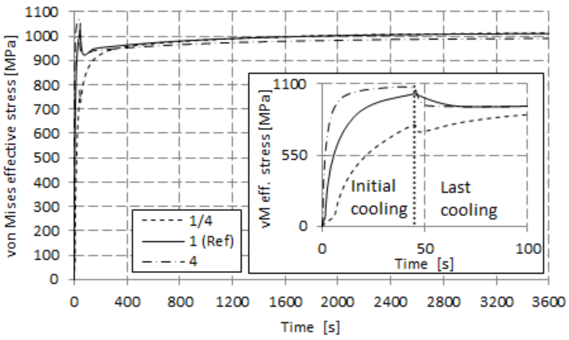

a) b)

Figure 18. a) Cooling rate profiles induced by different values of thermal conductivity and b) associated response in the evolution of the von Mises effective stress at a point in the mid-wall of the weld line.

4 Conclusions

This work presents an insight into the individual effects of the volumetric changes resulting from the thermal and transformation strain components and the interrelationship of these components on the build-up of residual stresses, given a set of material properties. IFW can be split into two stages, a welding stage (heating) and a cooling stage which is comprised of the initial and final cooling periods. The welding stage is characterized by low residual compressive stresses. Residual stresses are largely generated during the initial cooling period, when the total strain is dominated by inelastic thermal strains resulting from the fast cooling rates developed during this period. Across the weld interface, higher temperatures are experienced at the MD given the lower heat loses resulting from the absence of convection and radiation, and thus higher residual stresses are expected at the ID and OD. However, during the final cooling period most of the heat has been dissipated and the rate of change in temperature (*dT*/*dt*) reaches near constant values throughout the welded components and the total strain is no longer dominated by thermal strains. Therefore the significance of the cooling rates on the predicted final residual stress becomes negligible (<2%) as the process time approaches the end of the final cooling period. Notwithstanding, a fast cooling rate may lead to crack nucleation and crack growth in the initial cooling period and so this must be avoided in the manufacturing of IFW components. During the final cooling period however, in the IFW of CrMoV steels, the total strain is dominated by transformation strains rather than by thermal strains. Volumetric changes experienced in the lattice at the onset of transformation from austenite to martensite relax up to 70% of the stress level within the HAZ, and it is therefore significantly important for the accurate prediction of residual stresses to take into account the transformation strain component in the FE modeling of IFW. Additionally, the final residual stress state in the component is strongly sensitive to the interrelationship between the thermo-mechanical properties defining each of these phases, leading to higher residual stresses (>12%) in regions approaching the edge of the HAZ. The accumulation of residual stresses was shown to be more sensitive to material properties defining the elastic behavior rather than the plastic behavior, which can be attributed to the influence of elastic recovery during the final cooling period. This study has demonstrated the capability of a two-phase model, including only a harder tempered martensite phase at low temperatures and a softer austenite phase at high temperatures, but neglecting the quenched martensite phase to capture the evolution of residual stresses at the same level of accuracy and with a reduced amount of material data, which is difficult to obtain, compared to a three-phase model given the similarity in thermo-mechanical properties between martensite in the quenched and tempered state. In order to promote a most favorable state of stress within the HAZ, selecting a stick-out distance equal to a half of the workpiece is a good practice as this results in a better distribution of axial stresses and a better control of material flow in the radial and hoop direction, which in turn results in lower residual stresses within the HAZ.

5 References

Balasubramanian, V., Li, Y., Stotler, T., and Crompton, J., 1999. An energy balance method for the numerical simulation of inertia welding. Materials and Manufacturing Processes 14, 755-773.

Bennett, C.J., 2007a. Inertia Friction Welding of High Strength Aerospace Alloys, Department of Mechanical, Materials and Manufacturing Engineering. The University of Nottingham, Nottingham.

Bennett, C.J., Attallah, M.M., Preuss, M., Shipway, P.H., Hyde, T.H., and Bray, S., 2013. Finite Element Modeling of the Inertia Friction Welding of Dissimilar High-Strength Steels. Metallurgical and Materials Transactions A 44, 5054-5064.

Bennett, C.J., Hyde, T. H., Williams, E. J., 2007b. Modelling and simulation of the inertia friction welding of shafts. Journal of Materials Design and Applications 221, 275-284.

Bennett, C.J., Iracheta, O., Sun, W., 2014. Characterisation of mechanical property variation across an inertia friction weld of a CrMoV steel, TMS2014 Annual Meeting Supplemental Proceedings, San Diego, CA, USA., pp. 713-720.

Grant, B., Preuss, M., Withers, P.J., Baxter, G., and Rowlson, M. , 2009. Finite element process modelling of inertia friction welding advanced nickel-based superalloy. Materials Science and Engineering A 513-514, 366-375.

Kearns, W.H., 1980. Welding Handbook: Resistance and solid state welding and other joining processes. American Welding Society, Miami.

Kobayashi, S., 1989. Metal forming and the finite element method. Oxford University Press, New York, Oxford.

Lee, K., Samant, A., Wu, W.T., Srivatsa, S., 2001. NUMIFORM.

Lippold, J.C., Odegard, B.C., 1984. Microstructural Evolution During Inertia Friction Welding of Austenitic Stainless Steels. Welding Journal 63, 35s-38s.

Maalekian, M., 2007. Friction welding - critical assesment of literature. Science and technology of welding and joining 12, 738-759.

Messler, R.W., 1942. Joining of materials and structures : from pragmatic process to enabling technology. Butterworth-Heinemann, Boston ; Oxford

Moal, A., Massoni, E., 1995. Finite element simulation of the inertia welding of two similar parts. Engineering Computations 12, 497-512.

Moat, R., Karadge, M., Preuss, M., Bray, S., and Rawson, M., 2008. Phase transformations across high strength dissimilar steel inertia friction weld. Journal of Materials Procssing Technology 204, 48-58.

Mohammed, M.B., 2011. Process modelling of inertia friction welding process using finite element analysis, Department of Mechanical, Materials and Manufacturing Engineering. The University of Nottingham, Nottingham.

Mohammed, M.B., Bennett, C.J., Shipway, P.H., and Hyde, T.H., 2010. Optimization of Heat Transfer in the Finite Element Process, Heat Transfer 2010, Tallinn, Estonia.

Rich, T., Roberts, R., 1971. The forging phase of friction welding. Metal construction and British welding journal, 93-98.

Rykalin, N.N., Pugin, A. I. and Vasil'eva, V. A. , 1959. The Heating and Cooling of Rods Butt Welded by the Friction Process. Svarochnoe Proizvodstvo (Welding Production), 42-52.

SFTC, 2011. DEFORM v10.2 and DEFORM v11.0 (Beta) Integrated 2D3D system manual, in: Fluhrer, J. (Ed.), Columbus, Ohio.

Tabor, D., 1951. The hardness of metals. Oxford University Press, Oxford.

Vill, V.I., 1959. Energy Distribution in the Friction Welding of Steel Bars. Welding Production, 31-41.

Wang, K.K., Nagappan, P., 1970. Transient Temperature Distribution in Inertia Welding of Steels. Welding Journal 49, 419 - 426.

Wang, L., Preuss, M., Withers, P.J., Baxter, G. Wilson, P., 2005. Energy-input-based finite-element process modeling of inertia welding. Metallurgical and materials transactions B 36B, 513-523.